The Submesoscale Kinetic Energy Cascade: Mesoscale Absorption of Submesoscale Mixed Layer Eddies and Frontal Downscale Fluxes

René Schubert

GEOMAR Helmholtz Centre for Ocean Research Kiel, Kiel, Germany

Jonathan Gula

Univ. Brest, CNRS, IRD, Ifremer, Laboratoire d'Océanographie Physique et Spatiale, IUEM, Brest, France

Richard J. Greatbatch

GEOMAR Helmholtz Centre for Ocean Research Kiel, and Christian-Albrechts-University Kiel, Kiel, Germany

Burkard Baschek

Helmholtz Centre for Materials and Coastal Research, Geesthacht, Germany

Arne Biastoch

GEOMAR Helmholtz Centre for Ocean Research Kiel, and Christian-Albrechts-University Kiel, Kiel, Germany

ABSTRACT

Mesoscale eddies can be strengthened by the absorption of submesoscale eddies resulting from mixed layer baroclinic instabilities. This is shown for mesoscale eddies in the Agulhas Current system by investigating the kinetic energy cascade with a spectral and a coarse-graining approach in two model simulations of the Agulhas region. One simulation resolves mixed layer baroclinic instabilities and one does not. When mixed layer baroclinic instabilities are included, the largest submesoscale near-surface fluxes occur in wintertime in regions of strong mesoscale activity for upscale as well as downscale directions. The forward cascade at the smallest resolved scales occurs mainly in frontogenetic regions in the upper 30 m of the water column. In the Agulhas ring path, the forward cascade changes to an inverse cascade at a typical scale of mixed layer eddies (15 km). At the same scale, the largest sources of the upscale flux occur. After the winter, the maximum of the upscale flux shifts to larger scales. Depending on the region, the kinetic energy reaches the mesoscales in spring or early summer aligned with the maximum of mesoscale kinetic energy. This indicates the importance of submesoscale flows for the mesoscale seasonal cycle. A case study shows that the underlying process is the mesoscale absorption of mixed layer eddies. When mixed layer baroclinic instabilities are not included in the simulation, the open-ocean upscale cascade in the Agulhas ring path is almost absent. This contributes to a 20% reduction of surface kinetic energy at mesoscales larger than 100 km when submesoscale dynamics are not resolved by the model.

1. Introduction

The ocean moves on temporal and spatial scales ranging from the global thermohaline overturning circulation to the microscale turbulent motion of single fluid particles. The amount and scale distribution of the associated kinetic energy is mainly controlled by the balance between atmospheric forcing and oceanic dissipation and cross-scale energy fluxes (Ferrari and Wunsch 2009). Atmospheric wind and buoyancy forcings mainly act on the large scales. A part of this energy is dissipated to heat at molecular scales at the sea surface or transferred back to the atmosphere through intense atmosphere–ocean interactions

---

ⓐ Denotes content that is immediately available upon publication as open access.

Corresponding author: René Schubert, rschubert@geomar.de

(e.g., Ma et al. 2016; Renault et al. 2016). The rest of the energy input is dissipated in the ocean interior or at coastlines and the sea floor. Key questions are how the energy is transported from the large scales to the dissipative scale (the "forward cascade") and how the scale distribution of kinetic energy and its temporal evolution are shaped (see review in Klein et al. 2019). Large-scale ocean currents like the Gulf Stream, the Kuroshio, or the Agulhas Current undergo mixed baroclinic–barotropic instabilities associated with the shedding of mesoscale eddies that act as a source of energy at the mesoscale (e.g., Cronin 1996; Storch et al. 2012; Schubert et al. 2018). Satellite altimetry revealed that the mesoscales are associated with an "inverse cascade," i.e., a transport of kinetic energy toward larger scales (Scott and Wang 2005). In combination with the large-scale energy sources of the ocean, this inverse cascade results in the larger mesoscale eddy field being the most energetic scale band of the ocean (Ferrari and Wunsch 2009). From altimetric data interpolated onto a regular grid by AVISO (Archiving, Validation, and Interpretation of Satellite Oceanographic Data, www.aviso.altimetry.fr), Scott and Wang (2005) found for the South Pacific, and Scott and Arbic (2007) for the Kuroshio extension, that the upscale kinetic energy flux changes to a downscale cascade around the wavelength λ_r of the Rossby radius of deformation. It is given by $\lambda_r = 2\pi R_r$, where R_r is the Rossby radius of deformation, and is about 170 km in the midlatitudes (Chelton et al. 1998). Tulloch et al. (2011) found similar results from satellite altimetry as well as from a coarse-resolution aquaplanet model. However, in ocean models with submesoscale permitting resolution ($\approx 1/30° \approx 4$ km at midlatitudes) the change from inverse to forward cascade occurs on smaller wavelengths of about 40 km (Arbic et al. 2013; Qiu et al. 2014). These studies showed that filtering the model results in space (Qiu et al. 2014), or both in space and time in a similar way as done in the AVISO postprocessing (Arbic et al. 2013), leads to spectral fluxes that are closer to those estimated from AVISO. This indicates that the scale fluxes from the altimetric measurements represent those of filtered mesoscale dynamics, while the submesoscale inverse kinetic energy cascade is not captured by the altimetric measurements. Qiu et al. (2014) attributed the submesoscale upscale kinetic energy transport to the inverse cascade of eddies resulting from mixed layer baroclinic instability. In their simulation, consistently a strong wintertime inverse cascade occurs extending down to scales of 35 km, while the summertime inverse cascade is much weaker and changes to a forward cascade already at wavelengths of 100 km. The wintertime value is close to ≈ 30 km, as also found by Klein et al. (2008) and Capet et al. (2008) for submesoscale-permitting simulations with

resolutions of 2 and 1.5 km, although the investigated oceanic regimes were different. Qiu et al. (2014) and Klein et al. (2008) investigated submesoscale turbulence in the region of a zonal baroclinically unstable jet, while Capet et al. (2008) addressed submesoscale flows in an upwelling region. Capet et al. (2008) found some evidence for convergence, as a similar wavelength was found for a 750-m horizontal resolution sensitivity experiment. In this paper, we attribute the submesoscale inverse kinetic energy cascade to the mesoscale absorption of the mixed layer eddies. We show that the submesoscale kinetic energy reaches the mesoscales with a few months delay which is the time the absorption needs to proceed. We further show that the scale at which the surface inverse cascade changes to a forward cascade depends on the local wavelength of the fastest growing mode of mixed layer baroclinic instability.

The forward cascade in the submesoscale resolving simulations of Capet et al. (2008) was attributed to the ageostrophic (horizontal divergent) part of the flow. Capet et al. (2008) hypothesized that frontogenesis and submesoscale frontal instabilities were the responsible processes at work. Supporting these results, D'Asaro et al. (2011) observed enhanced dissipation of kinetic energy at an oceanic front in the Kuroshio, and attributed it to symmetric instability. Molemaker and McWilliams (2010) and Barkan et al. (2015) also found a vigorous forward cascade associated with frontal instabilities in idealized model experiments. Here, we explicitly show that, in an ocean model, most of the downscale flux of kinetic energy at the small scales occurs in frontogenetic regions.

The representation of the mesoscale eddy field in ocean models depends on the part of the kinetic energy cascade that is resolved or parameterized. Kjellsson and Zanna (2017) showed that the upscale kinetic energy flux as well as the spectral kinetic energy density increase for all horizontal scales when the horizontal resolution of their global ocean model is increased from 1° to 1/4° and to 1/12°. Furthermore, Schubert et al. (2019) compared the non-submesoscale-resolving 1/20° (≈ 4.5 km) simulation "INALT20r" of the Agulhas region to the submesoscale-permitting 1/60° (≈ 1.5 km) simulation "INALT60," as well as to satellite altimetry measurements. They showed that, in the Cape Basin, INALT60 is associated with mesoscale power spectral densities of sea surface height that are similar to the observations, while INALT20r lacks power spectral density on all scales. In the present study, we build on Schubert et al. (2019) and investigate the kinetic energy cascade in the Agulhas region on the basis of these both simulations.
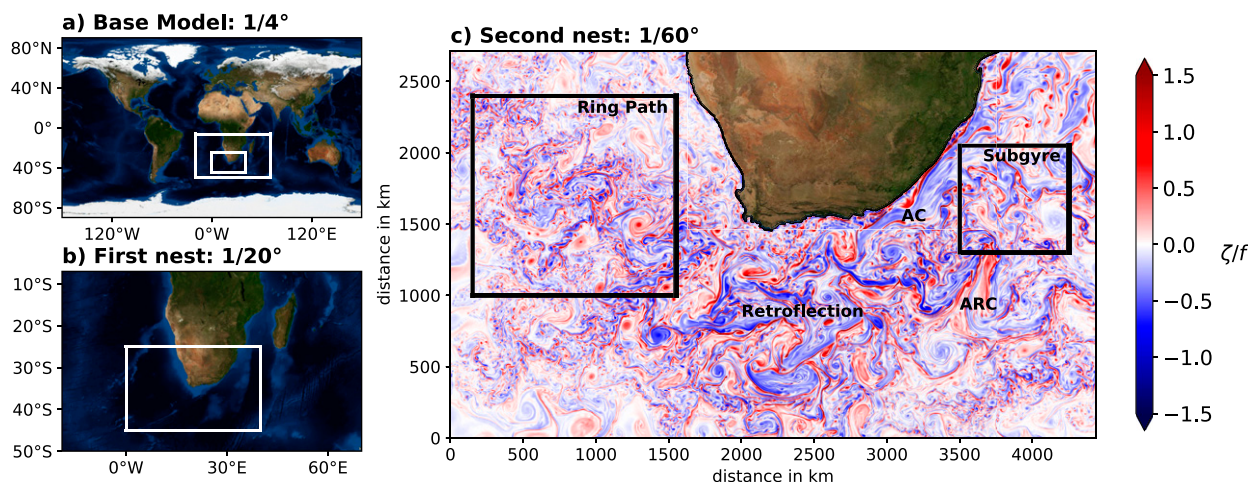
FIG. 1. INALT60: (a) a 1/4° horizontal resolution base model with (b) a first 1/20° nest and (c) a second 1/60° nest (c). In (c), a snapshot of the normalized surface relative vorticity ζ/f on model day 9 Sep 2012 is shown. The labels AC and ARC show the position of the Agulhas Current and the Agulhas Return Current, respectively. Land and bathymetry backgrounds are taken throughout the paper from Stöckli et al. (2005). White boxes in (a) and (b) show the location of the nests. Black boxes in (c) mark the regions of the computations for Figs. 2–4, 7, and 8.

The Agulhas region is associated with strong water mass exchanges between the Atlantic as well as Indian and Southern oceans. This exchange is of importance for the stratification in the South Atlantic (de Ruijter et al. 1999), the tropical Atlantic Ocean (Lübbecke et al. 2015), and the Atlantic meridional overturning circulation (Weijer et al. 2002; Biastoch et al. 2008, 2015). The main feature of the Agulhas region is the Agulhas Current (AC) flowing poleward along the African continental slope with a transport of about 77 Sv (1 Sv = $10^6\,m^3\,s^{-1}$) (Beal et al. 2015). South of Africa, the AC separates from the slope, retroflects to the east and continues as the Agulhas Return Current (ARC; Lutjeharms and Ansorge 2001). At the retroflection, anticyclonic Agulhas rings are shed and propagate northwestward into the Atlantic. Although a part of their water masses are mixed with their surroundings (Boebel et al. 2003), in particular by submesoscale currents (Capuano et al. 2018; Sinha et al. 2019), the Agulhas rings provide the largest portion of the "Agulhas leakage," which is the inflow of warm and salty Indian Ocean waters into the Atlantic (Lutjeharms 2007). Besides the anticyclonic Agulhas rings, southwestward propagating Agulhas cyclones are shed in the retroflection region (Lutjeharms et al. 2003). Further westward propagating eddies develop at the front of the Benguela upwelling system west of Africa (Rubio et al. 2009). All of these eddies strongly interact with the Agulhas rings in the Cape Basin (Boebel et al. 2003).

First, a short overview of both experiments, INALT60 and INALT20r, is presented in section 2. In section 3, the submesoscale kinetic energy cascade is investigated in order to understand the underlying processes. A discussion and a conclusion are presented in section 4.

2. The model experiments

In this study, we mainly analyze the output of the submesoscale-permitting numerical-model simulation INALT60. Its configuration has been introduced by Schwarzkopf et al. (2019) and was further developed by Schubert et al. (2019). The model grid consists of a global host grid with a 1/4° horizontal resolution and 120 vertical levels, a first horizontal grid refinement (nest) down to 1/20° ($\approx$4.5 km) for the greater Agulhas region and a secondary nest down to 1/60° ($\approx$1.5 km) for the core Agulhas region (Fig. 1). The primitive equations are solved on an Arakawa C grid (Arakawa and Lamb 1977) with NEMOv3.6 (Nucleus for European Modeling of the Ocean; Madec and NEMO Team 2016). The nesting is done with an Adaptive Grid Refinement in FORTRAN (AGRIF; Debreu et al. 2008) allowing for a two-way exchange of the model solution between the host and the nest grids. For the host grid and the first nest, explicit dissipation with a bi-Laplacian operator and a constant viscosity is used. The viscosity is quadratically scaled down from the host-grid value of -1.5×10^{11} to $-6 \times 10^9\,m^4\,s^{-1}$ for the first nest. For explicit tracer diffusion, a Laplacian operator with constant diffusivity is used in the host grid and the first nest. The diffusivity is linearly scaled down from the host-grid value of 300 to $60\,m^2\,s^{-1}$ for the first nest. For the discretization of the vorticity term, we use the vector invariant form with a Hollingsworth-corrected energy- and
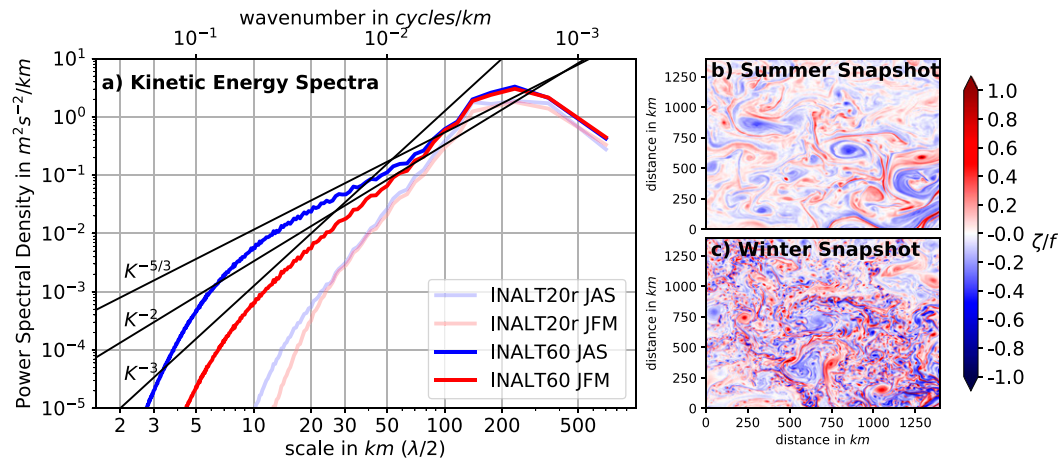
FIG. 2. (a) Winter (JAS; blue) and summer (JFM; red) mean surface kinetic energy spectra for the period 2012–17 in the ring path (western box in Fig. 1c) computed from INALT60 (solid) and from INALT20r (transparent). Straight black lines show spectral slopes of $K^{-5/3}$ (surface quasigeostrophy), K^{-2} (surface quasigeostrophy with ageostrophic advection), and K^{-3} (interior quasigeostrophy), where K is the isotropic wavenumber. Snapshots of normalized surface relative vorticity ζ/f from INALT60 are shown for the ring path for (b) 18 Jan 2012 (summer) and (c) 5 Aug 2012 (winter).

enstrophy-conserving scheme (Arakawa and Hsu 1990; Hollingsworth et al. 1983; Bell et al. 2017; Ducousso et al. 2017). For tracer advection, we apply the total variance dissipation scheme (Zalesak 1979).

In the second nest, no explicit diffusion and dissipation are used in combination with third-order upstream biased advection schemes (Webb et al. 1998; Farrow and Stevens 1995; Madec and NEMO Team 2016) for both tracer and momentum. For the 1/60° domain, the model output is written as daily means for the whole water column and as 4-h means for the upper 250 m. Moreover, for the upper 250 m, a model snapshot is written every fifth day at 1200 UTC. A comprehensive validation of INALT60 shows in particular in the ring path a very good agreement with satellite and in situ observations on all simulated scales (Schubert et al. 2019).

The results from INALT60 are compared to a parallel experiment that is identically but without the secondary nest. This experiment resolves almost no submesoscale flows. Schubert et al. (2019) also describe this experiment in detail and refer to it as INALT20r.L120.HighDiff. The acronym stands for 1/20° horizontal resolution, 120 vertical levels, and relatively high diffusion and dissipation settings (see above). Here, we call it INALT20r for simplicity. The "r" emphasizes that the configuration is associated with a reduced nested domain compared to INALT20 (see Schwarzkopf et al. 2019 for details). Both experiments are integrated from 2010 to 2017. They are initialized from the same 30-yr spinup of a similar INALT20r configuration that used only 46 vertical levels and CORE2 forcing (Large and Yeager 2009;

Griffies et al. 2009), while both experiments analyzed here use 120 vertical levels and the better resolved (1/2°, 3-hourly) JRA55-do forcing (v1.3, Tsujino et al. 2018). For more details on the simulations and configurations, we refer to Schubert et al. (2019) and Schwarzkopf et al. (2019).

3. Results

First, we analyze the surface kinetic energy as a function of spatial scale and season in the ring path. The 2012–17 mean horizontal wavenumber spectra of surface kinetic energy[1] in INALT60 for summer (JFM) and winter (JAS) peak, in the ring path, at a scale of 200 km (Fig. 2a). In the mesoscale range of between 80 and 130 km, they drop with a slope close to the interior quasigeostrophic prediction of K^{-3} (Charney 1971; Lapeyre and Klein 2006), where K is the isotropic horizontal wavenumber. At smaller scales, the spectrum changes depending on the season. In summer, the small-scale dynamics are dominated by fronts, in particular between the mesoscale eddies and only a few submesoscale vortices (Fig. 2b). The summer spectrum continues at the smaller scales with a slope of about K^{-3} down to 7 km, where the spectrum drops due to the dominant effect of the model dissipation. A scale of 7 km can thus be identified as the effective resolution of INALT60. The respective wavelengths (14 km) is

---

[1] See appendix A for details on the computation of the kinetic energy spectra.

about 10 times the grid spacing (1.5 km), consistent with Soufflet et al. (2016). In winter, the ring path is associated with many small-scale vortices and fronts that are strongest along the boundaries of the meso-scale eddies (Fig. 2c). Compared to summer, the winter spectrum is associated with more energy at scales smaller than 75 km, as it follows a shallower slope that is close to the predictions of surface quasigeostrophic theory ($K^{-5/3}$; Blumen 1978; Held et al. 1995; Lapeyre 2017). The comparison of the kinetic energy spectral slope to the theoretical predictions suggest that, in the ring path, the mesoscale and summer submesoscale dynamics, follow an interior quasigeostrophic regime and the winter submesoscale dynamics follow a surface quasigeostrophic regime. However, the simulated sub-mesoscale flows are associated with Rossby numbers[2] of about 1–3 (Schubert et al. 2019). Thus, the flow deviates from quasigeostrophic balance and is associated with relevant ageostrophic components. If ageostrophic advection, or a mixed layer, is included in surface quasigeostrophy, a steeper slope of K^{-2} is predicted (Boyd 1992; Callies and Ferrari 2013). In this regard, it is surprising that the slope is much closer to $K^{-5/3}$ than to K^{-2}. Further, in this paper, we show that the mixed layer baroclinic instability is important for the submesoscale kinetic energy cascade. The original surface quasigeostrophic theory (Blumen 1978), however, does not account for the mixed layer and associated instabilities and thus cannot describe the submesoscale dynamics we address in this study.

In the non-submesoscale-resolving simulation INALT20r, the kinetic energy spectra are similar in both seasons with less energy than in INALT60 at almost all scales and a slope steeper than the interior quasigeostrophic predictions (Fig. 2a). The fact that the mesoscale dynamics are weaker in INALT20r compared to INALT60 indicates that the resolved submesoscale flows strengthen the mesoscales in INALT60. To address this strengthening further, the scale kinetic energy flux is investigated in the following. The scale kinetic energy flux is the transfer rate of kinetic energy through a specific horizontal scale from currents of smaller horizontal scales to currents of larger horizontal scales. Classically, the scale kinetic energy flux is computed based on Fourier transformation in spectral space (e.g., Scott and Wang 2005). Here, we use an alternative coarse-graining approach based on Leonard (1975),

Germano (1992), Eyink (2005), and Aluie et al. (2018). Both approaches and respective computations are described in detail in appendix B. As this is, as far as we know, the first study that applies the coarse-graining approach to a submesoscale-permitting ocean general circulation model output, in the following, the results are compared to the classical spectral approach.

The results for the surface scale kinetic energy flux computed with both approaches are very similar in the ring path (Fig. 3). The fluxes are directed toward larger scales (negative) for most of the investigated scales. The scale flux is larger in winter than in summer for almost all scales and for both upscale and downscale directions (Fig. 3c). The surface inverse cascade changes to a forward cascade at scales of around 13 km in winter and about 25 km in summer. The agreement between results from both approaches is particularly good at scales smaller than 30 km. At larger scales, the spectral flux is weaker and noisier than the coarse-graining flux. We hypothesize that the assumption of homogeneous and isotropic turbulence, made for the spectral approach, particularly produces erroneous results at larger scales. Contrary to the spectral approach, the coarse-graining approach does not require windowing the signal at the boundaries of the domain. For comparison, the coarse-graining flux is windowed in a similar way as the horizontal velocity components are windowed for the spectral flux computation. For that, a two-dimensional Hanning window of the same size and the associated correcting factor of 1.5 are multiplied to each horizontal field of the coarse-graining flux, before it is spatially averaged.[3] In the ring path, the nonwindowed coarse-graining flux is about twice as large as the windowed flux (Fig. 3c) pointing out the damaging impact that windowing velocities can have on the computation of the scale kinetic energy flux.

To attribute the scale kinetic energy flux to particular processes, first, the depth distribution of the spatially averaged winter scale kinetic energy flux in the upper 250 m of the ring path is addressed. We restrict the analysis to a single model snapshot that is representative for the winter season, as the computational costs for the flux computations are very large. At the surface of the ring path, the winter inverse cascade reaches down to about 13 km (Fig. 4a), which is consistent with Fig. 3. Below 50-m depth, the change of inverse to forward cascade occurs below 7 km, indicating that a small part of the inverse cascade is still not resolved by the simulation.

---

[2] The Rossby number (Ro) is defined as Ro = $|\zeta/f|$, where $\zeta = v_x - u_y$ is the vertical component of the relative vorticity with the meridional velocity component v and the zonal component u and $f = 2\Omega \sin(\varphi)$ is the planetary vorticity with Earth's rotation rate $\Omega = 7.2921 \times 10^{-5}$ rad s^{-1} and the latitude φ.

[3] This method is a compromise with respect to computational power. For a very clean comparison, the coarse-graining method would need to be applied to the windowed fields of the horizontal velocity components.
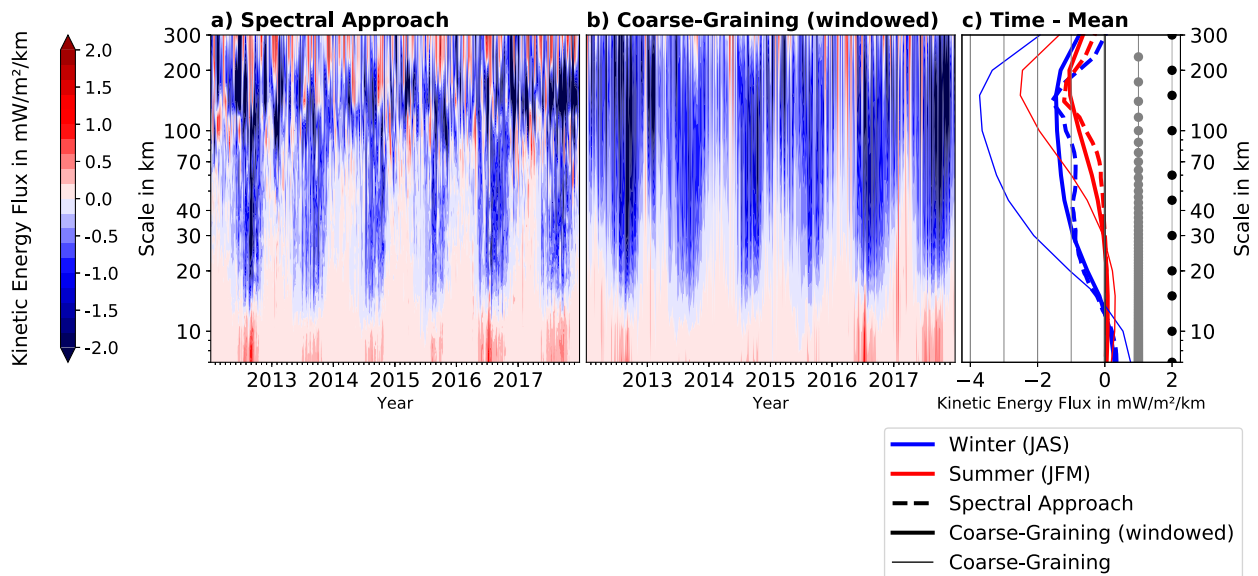
FIG. 3. The surface scale kinetic energy flux as a function of time and scale in the Agulhas ring path of INALT60 (western box in Fig. 1c) computed with (a) the spectral approach and (b) the coarse-graining approach. The results are shown for model snapshots every fifth day. Note that for comparison, the coarse-graining flux is windowed similarly to the velocity components before the spectral flux computations and is subsequently averaged in space. (c) The winter (blue; JAS) and summer (red; JFM) mean fluxes are shown for the windowed coarse-graining (thick, solid), the nonwindowed coarse-graining (thin, solid) and the spectral approach (thick, dashed). Black and gray dots in (c) mark for which scales the fluxes are computed. The scale is identified as half the wavelength for the spectral flux and as the diameter L of the smoothing kernel G for the coarse-graining flux.

Both the downscale and upscale contributions to the total kinetic energy fluxes are surface intensified (Figs. 4b,c). The downscale flux is concentrated in the upper 30 m and shows a maximum at scales around 15 km (Fig. 4b).

The upscale flux fills the entire mixed layer (the top 100 m) and increases with the scale (Fig. 4c).

Downscale fluxes occur at small scales mainly in frontogenetic regions. A wintertime snapshot of the simulated
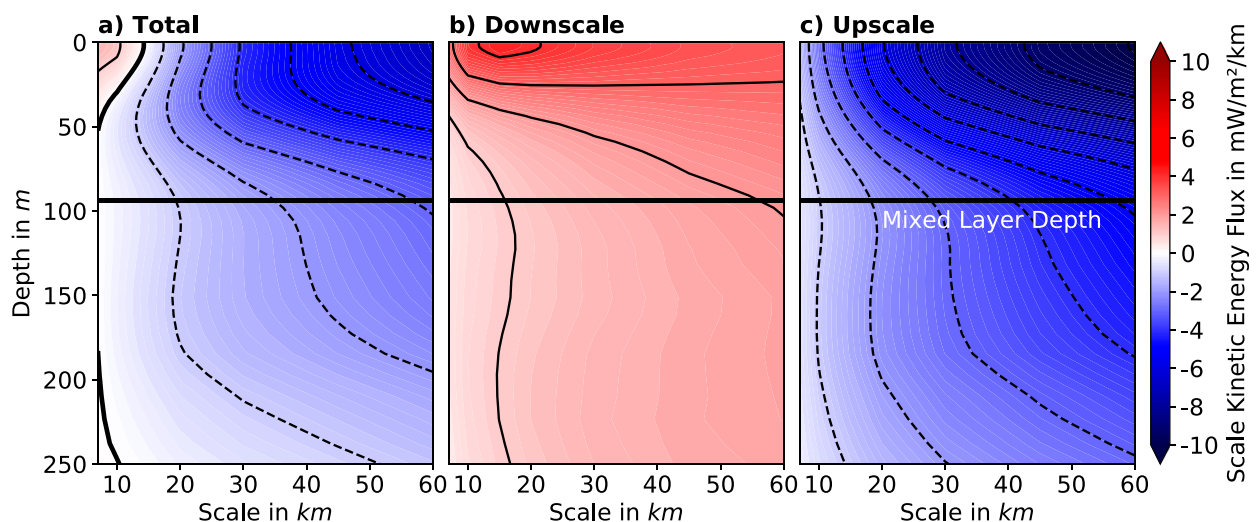

FIG. 4. (a) The spatial-mean scale kinetic energy flux (shading and contours with an interval of 1 mW m^{-2} km) computed with the coarse-graining approach from a winter model snapshot (4 Sep 2012) for the ring path of INALT60 (western box in Fig. 1c). (b) Downscale and (c) upscale contributions to the total flux are shown. They are computed by setting the negative and positive fluxes, respectively, to zero before spatial averaging and add up to the total flux. Black horizontal lines show the spatial mean mixed layer depth.

a) Surface Density

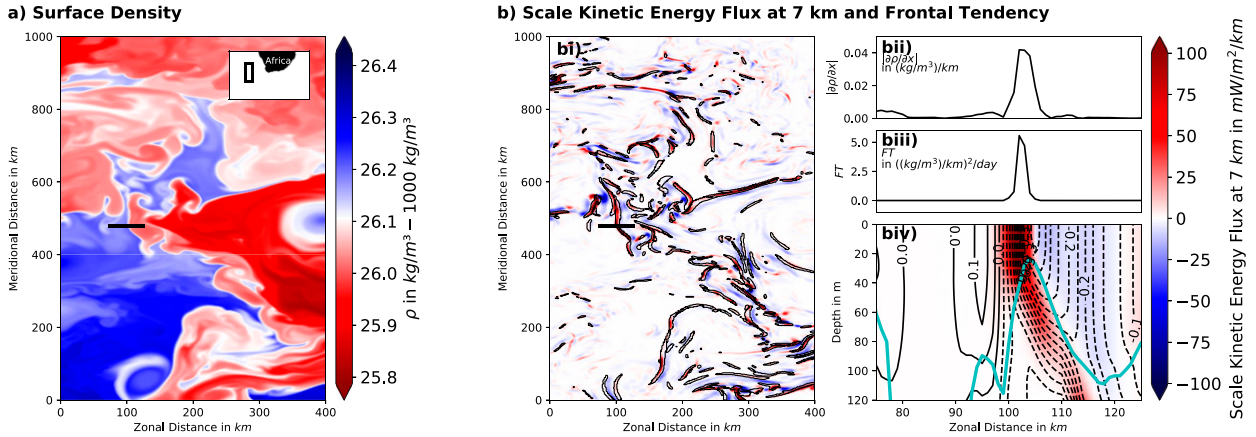**b) Scale Kinetic Energy Flux at 7 km and Frontal Tendency**

FIG. 5. Downscale fluxes occur at small scales mainly in frontogenetic regions: (a) an INALT60 snapshot (4 Sep 2012) of surface density and (b) the surface scale kinetic energy flux at 7 km computed with the coarse-graining approach overlaid by the 0.1 [(kg m^{-3}) km^{-1}]^2 day^{-1} frontogenetic tendency contour (bi) in the region shown in the small map in (a). The zonal black line in (a) and (bi) shows the location for which in (bii), the absolute value of the surface zonal density gradient, in (biii) the surface frontal tendency and in (biv) a vertical section of the scale flux at 7 km (shading) and the meridional velocity (contours with an interval of 0.025 m s^{-1}—dashed southward and solid northward) are shown. The cyan line in (biv) marks the mixed layer depth.

surface density in the ring path of INALT60 shows the presence of sharp density fronts (Fig. 5a). Positive values of the frontal tendency,

$$\text{FT} = -[\rho_x^2 u_x + \rho_y^2 v_y + \rho_x \rho_y (u_y + v_x)],$$

here computed following Hoskins (1982) with the potential density ρ and associated derivatives, mark frontogenetic regions. For the snapshot, most of the surface downscale fluxes at 7 km occur in frontogenetic regions with FT > 0.1 [(kg m^{-3}) km^{-1}]^2 day^{-1} (Fig. 5b). A vertical section through a front shows that the downscale flux occurs mainly at the frontogenetic flank of the frontal jet (Figs. 5bii–iv). The downscale flux occurs mainly in the upper 30 m, consistent with Fig. 4b. Similar results are found for the whole (1/60)° domain. In the model output snapshots every fifth day for the whole 1/60° domain of INALT60 and the time period 2012–17, 61% of the surface downscale flux at a scale of 7 km occur in frontogenetic regions with FT > 0.1 [(kg m^{-3}) km^{-1}]^2 day^{-1}. This indicates that frontogenesis and frontal processes such as frontal instabilities are key elements of the forward cascade.

In the remainder of the paper, we present evidence that the upscale flux is attributable to the mesoscale absorption of mixed layer eddies. Mixed layer eddies develop as a consequence of mixed layer baroclinic instability that transfers potential energy of a mixed layer front to kinetic energy of the mixed layer eddies. A measure of the respective energy transfer is the vertical buoyancy flux VBF = $\rho_0 w' b'$, where $\rho_0 = 1024$ kg m^{-3} is the reference density, w is the vertical velocity component,

and $b = -g/\rho_0(\rho)$ is the buoyancy with the gravitational acceleration $g = 9.81$ m s^{-2}. Dashes mark deviations from the respective monthly mean. The available potential energy of a front increases with its vertical extent. In winter, when the mixed layer is deepest, the vertical extent of the fronts is largest and thus the available potential energy that can be transformed into kinetic energy is largest. Consequently, the submesoscale kinetic energy is largest in winter (consistent with Fig. 2) and much more mixed layer eddies occur (Figs. 2b,c). Indeed, most of the latter are not present in summer (Fig. 2b). Thus, they have to disappear within several months due to either dissipation or due to absorption by larger scale features. Here, we find indications that the latter is the case. A first indication that the submesoscale inverse kinetic energy cascade can be attributed to submesoscale mixed layer eddies is provided by the fact that it is strongest in winter for scales between 13 and 75 km (Fig. 3).

Second, a characteristic case study on the process of mixed layer instabilities and the subsequent mesoscale absorption of the associated submesoscale features by an Agulhas ring is presented. We investigate the dynamics and the scale kinetic energy flux on the basis of a series of snapshots. On model day 19 June 2012, the lighter waters of a warm-core, anticyclonic Agulhas ring are separated by a sharp density front from denser water east of the ring (Fig. 6a). South of the ring, submesoscale, high-Rossby-number features (Fig. 6e) and positive VBF at 60-m depth (Fig. 6i) indicate the activity of mixed layer instability in this part of the front. Five days later, the whole front east of the ring is associated with strong positive VBF (Fig. 6j) as well as mixed layer
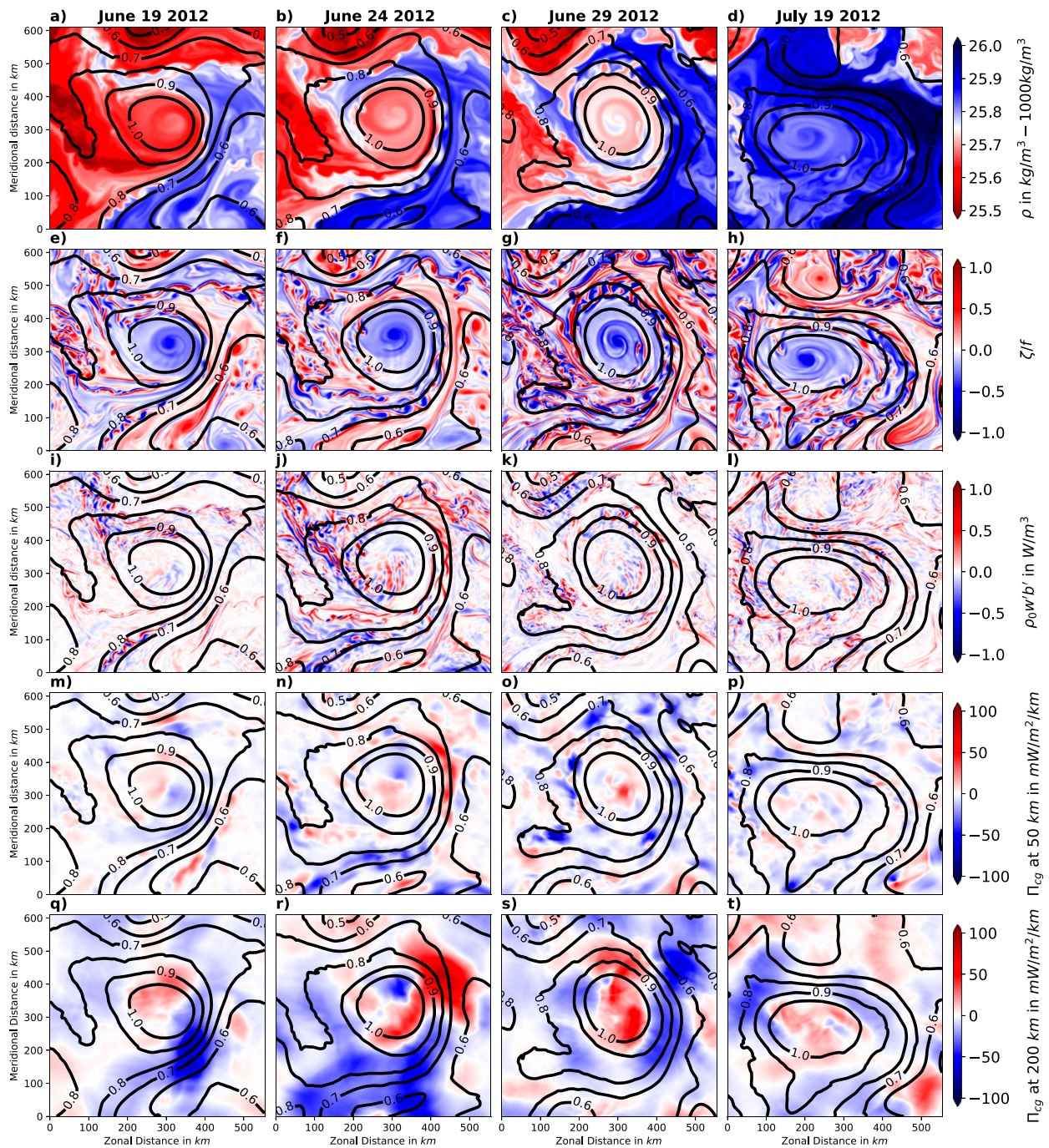
FIG. 6. The absorption of mixed layer instability generated features by an Agulhas ring in INALT60: (a)–(d) snapshots of surface density, (e)–(h) surface normalized relative vorticity, (i)–(l) vertical buoyancy flux at 60-m depth, and of surface scale kinetic energy flux at (m)–(p) 50 and (q)–(t) 200 km overlaid by sea surface height contours (m).

instability driven submesoscale features with a scale of about 40 km (Fig. 6f). At this stage, the southern boundary of the ring is associated with large upscale kinetic energy fluxes into scales of 50 km as well as into 200 km and thus into the scale of the ring. Downscale fluxes northeast of the ring might be driven by a squeezing of the ring due to the

northwestward advection of denser waters in this region (Figs. 6a,b). Another five days later, the whole ring as well as its boundary are associated with only weak VBF (Fig. 6k). The mixed layer instability has abated and the resulting submesoscale features are present along the whole boundary of the ring (Fig. 6g). This boundary is at
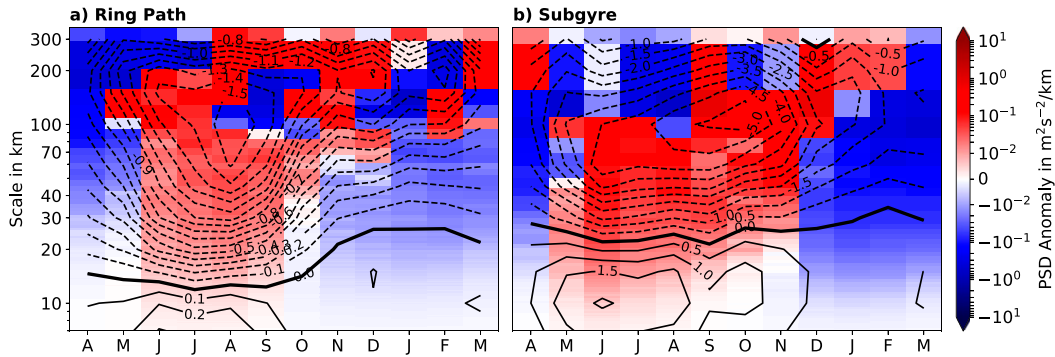
FIG. 7. Monthly climatology of the surface kinetic energy spectrum referenced to the mean spectrum ($m^2\,s^{-2}\,km^{-1}$; shading) and of the windowed and spatially averaged surface scale kinetic energy flux ($mW\,m^{-2}$; contours) for the period 2012–17 in (a) the Agulhas ring path and (b) the subgyre (the regions are marked with solid boxes in Fig. 1c). Note that the month axis starts with April to better visualize the upscale shift of the maximum in flux and power spectral density after the submesoscale season.

this stage associated with strong upscale fluxes into scales larger than 50 km and also into scales larger than 200 km indicating that the submesoscales flux their kinetic energy into the ring. In the center of the ring, downscale fluxes occur (Figs. 6o,s). These downscale fluxes might be related to frontogenesis within the ring (Fig. 6g). Another 20 days later on 19 July, and thus a month after the initialization of the frontal instability, the density contrast of the surface ring and its surrounding (Fig. 6d) as well as the sub-mesoscale flows around its boundary are much weaker (Fig. 6h). The boundary of the ring is still associated with upscale flux into scales larger than 200 km (Fig. 6t). This indicates that the absorption of the submesoscale features by the ring is still ongoing.

Third, as the absorption needs time to take effect, the submesoscale kinetic energy of the mixed layer eddies reaches the mesoscales with a delay. To investigate this, the monthly climatology of the scale kinetic energy flux is compared with the anomaly of the kinetic energy spectrum (Fig. 7a). The annual mean is subtracted from the monthly climatology to highlight the seasonal cycle of kinetic energy. Consistent with the previous results, the kinetic energy at scales smaller than about 75 km is strongest in winter, between June and September. At the largest mesoscales, the kinetic energy is strongest in August to December. The same shift is found for upscale kinetic energy flux: the maximum upscale flux occurs in August at scales of 90 km and shifts to larger scales around 200 km in November. In the ring path, the seasonal cycle of the mesoscales between 100 and 200 km is rather patchy, as it is disturbed by the irregular shedding of Agulhas rings and cyclones. Another hotspot of mesoscale eddy activity in the Agulhas region is the region east of the AC and north of the ARC, which we call the subgyre region. There, mesoscale eddies detach from the ARC and interact with those arriving from the south

Indian Ocean as well as with features that detach from the AC (Lutjeharms 2007). In the subgyre, the kinetic energy spectra in INALT20r show also less energy on all scales compared to INALT60 and the depth distribution of the wintertime scale flux in INALT60 shows similar patterns as presented in Fig. 4 for the ring path (not shown). Similar to the ring path, the maximum in me-soscale kinetic energy occurs a few months after the maximum in submesoscale kinetic energy and the re-spective shift is coincident with a shift of the maximum upscale flux (Fig. 7b). In contrast to the ring path, the coincidence of the seasonal cycles of kinetic energy and upscale flux is found for all scales. Further, in the sub-gyre, the submesoscale kinetic energy reaches the me-soscales in summer (DJF) and thus later than in the ring path. Our results indicate that the submesoscale-related upscale kinetic energy flux contributes to the seasonal cycle of mesoscale kinetic energy in both regions.

Fourth, the largest sources for the surface and wintertime inverse cascade are found at typical scales of features that result from the mixed layer instabil-ity. Stone (1970) extended the baroclinic instability model of Eady (1949) by ageostrophic perturbations and derived the wavelength of its fastest growing mode to be

$$\lambda_s = \frac{2\pi u_0}{|f|}\sqrt{\frac{1+\mathrm{Ri}}{5/2}}, \qquad (1)$$

where u_0 is the magnitude of the change in the thermal wind across the mixed layer and Ri the Richardson number. Typical values for the baroclinic instability of a midlatitude mixed layer front, $u_0 = 0.05\,\mathrm{m\,s^{-1}}$, $f = 7.29 \times 10^{-5}\,\mathrm{s^{-1}}$, and Ri $= 1$, give $\lambda_s = 3.9\,\mathrm{km}$ (Fox-Kemper et al. 2008). Using the thermal wind $u_0 = |\nabla_h b| h/f$, with the mixed layer depth h, in (1) gives
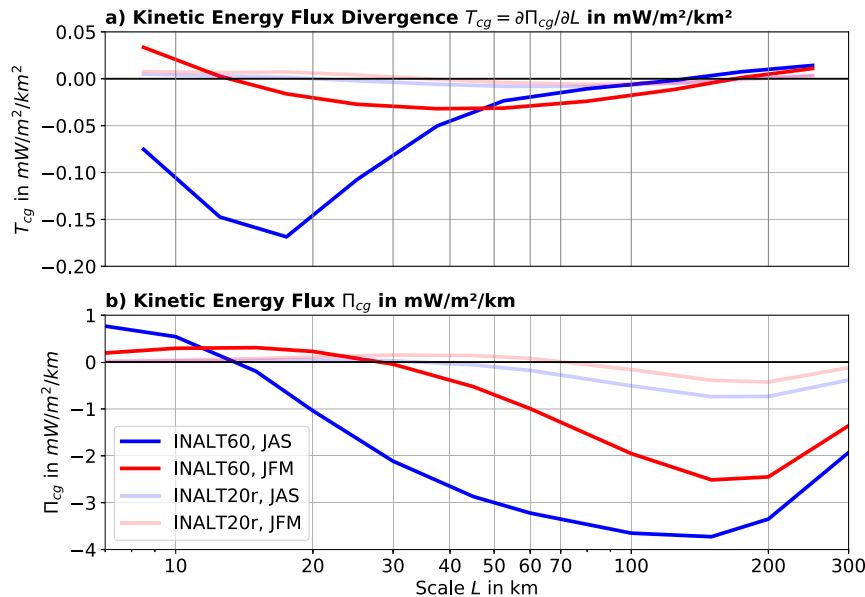
FIG. 8. (a) The divergence with respect to scale of the winter (blue; JAS) and summer (red; JFM) 2012–17 (b) mean surface scale kinetic energy flux in the Agulhas ring path (western box in Fig. 1c) computed with the coarse-graining approach (not windowed before spatial averaging) from INALT60 (solid) and INALT20r (transparent).

$$\lambda_s = \frac{2\pi|\nabla_h b|h}{f^2}\sqrt{\frac{1+\mathrm{Ri}}{5/2}}. \qquad (2)$$

Fox-Kemper et al. (2008) showed with an idealized nonlinear model simulation that the linear theory captures the growth of the perturbations only in the first six days after initialization. After the instabilities reached finite amplitude, they observed a nonlinear transfer of kinetic energy to scales larger than the most unstable wavelength to scales of 15 km and larger. These are the scales where the source of the upscale kinetic energy flux is found to be largest in the ring path of INALT60 in winter (Fig. 8a) and where the cascade changes from inverse to forward (Fig. 8b). The source of the upscale flux is computed here as the divergence of the scale kinetic energy flux with respect to the scale. At the same scales, also the slope of the winter-mean kinetic energy spectrum changes from $K^{-5/3}$ at scales of 15–75 km to steeper slopes of about K^{-3} and steeper at smaller scales (Fig. 2). This and the former are in agreement with the theoretical findings of Kraichnan (1967). For idealized turbulence he shows that, if kinetic energy is supplied continuously at a specific scale, at larger scales an energy inertial range develops with a $K^{-5/3}$ slope and an inverse cascade and at smaller scales an enstrophy inertial range with a steeper K^{-3} slope and a forward cascade. The agreement indicates that his considerations are valid for the submesoscale turbulence with an injection of kinetic energy through mixed layer instability at scales around 15 km.

A convergence for the inverse cascade is found for mesoscales larger than 130 km in winter and 190 km in summer. This is consistent with the notion that the mesoscale eddies, that are associated with these scales, absorb the mixed layer eddies. This provides a large scale limit to the part of the inverse cascade that is attributable to the submesoscale mixed layer dynamics. The inverse cascade attributable to the mesoscale eddies (eddy merging etc.), however, persists at these large scales. Processes that finally arrest the inverse cascade at even larger scales, such as for example barotropization and subsequent bottom drag or Rossby wave excitation (e.g., Rhines 1975; Tulloch et al. 2011), may also contribute to the convergence of the inverse cascade observed here.

Fifth, most of the sources for the inverse cascade are missing in INALT20r where the baroclinic mixed layer instability is not resolved (Fig. 8a). In the ring path in both winter and summer seasons, this means that about 7 times more kinetic energy is fluxed from the smaller scales to scales larger than 100 km in INALT60 (Fig. 8b). This intensified upscale energy flux contributes to a 28% increase in the mean surface kinetic energy in the ring path at scales larger than 100 km (computed from the velocity components that were smoothed with a 100-km diameter top-hat kernel) in INALT60. This is consistent with the increase of mesoscale SSH power spectral density reported by Schubert et al. (2019) when the mixed layer instability is resolved.
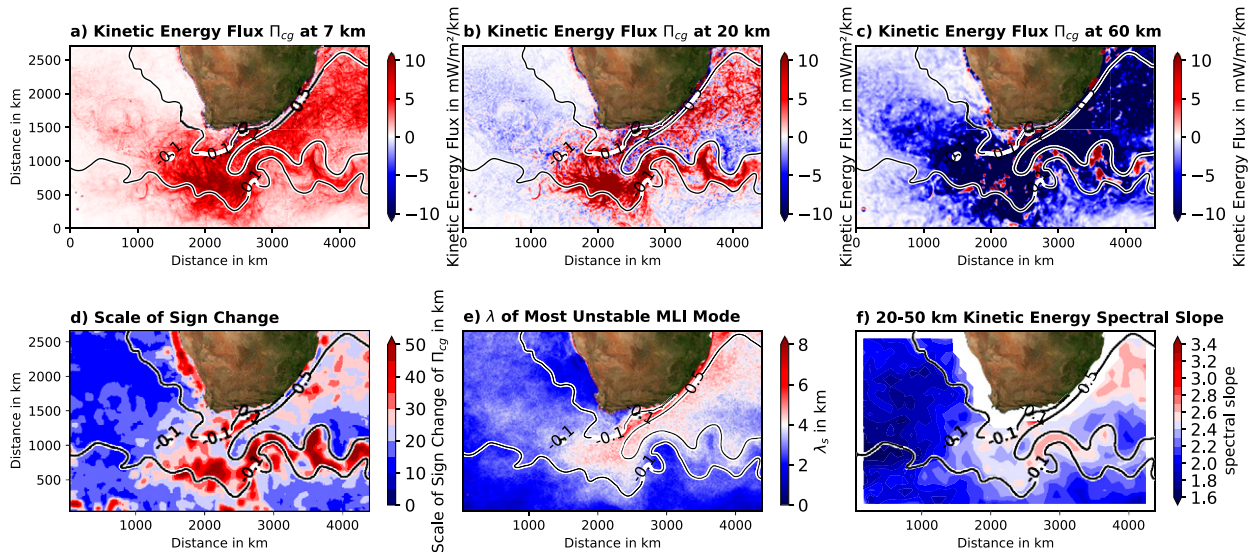
FIG. 9. The 2012–17 time-mean surface scale kinetic energy flux Π_{cg} computed from 4-h-mean outputs of INALT60 for (a) 7-, (b) 20-, and (c) 60-km scales. Blue (red) colors show downscale (upscale) fluxes. (d) The scale where the 2012–17 winter-mean (JAS) kinetic energy flux changes from down- to upscale computed from 4-h-mean INALT60 data. For (d), the very patchy original field has been smoothed with a 100-km diameter top-hat kernel. (e) The most unstable wavelength in the mixed layer (λ_s computed for 30-m depth) averaged from 2012 to 2017 over the winter months (JAS) from 5-day snapshots of INALT60. (f) The mean slope of the winter (JAS) mean surface kinetic energy spectrum from INALT60 for the period 2012–17 in the scale band 20–50 km. The average slope n with respect to K^{-n} is shown. For (f), for every 100 km in both horizontal directions, a mean kinetic energy spectrum is computed for a 350 km × 350 km subregion. Selected contours of the respective average of sea surface height highlight the location of the Agulhas Current system.

Sixth, the pattern of the scale at which the surface inverse cascade changes to forward is similar to the one of the wavelength of the most unstable mode of the mixed layer instability, as well as the one of the kinetic energy spectral slope. The 2012–17 time-mean surface scale kinetic energy flux in INALT60 is almost everywhere downscale at a scale of 7 km (Fig. 9a) and at 60 km almost everywhere upscale (Fig. 9c). The map of the flux at 20-km scales (Fig. 9b) highlights that the change from upscale to downscale occurs at different scales: In the retroflection, the subgyre and the ARC, the flux at a scale of 20 km is downscale, while in other regions, like the ring path, it is upscale. The winter-mean (JAS) surface scale kinetic energy flux changes from down to upscale in the Agulhas ring path at around 15 km, in the subgyre at around 25 km and in the retroflection and the ARC at even larger scales of 35–50 km (Fig. 9d). The pattern of the winter mean λ_s computed with Eq. (2) using Ri = 1 at a depth of 30 m in INALT60 (Fig. 9e) is, apart from the AC and ARC, similar to the one of the scale where the scale kinetic energy flux changes its sign. Moreover, both patterns are similar to the one of the 20–50-km spectral slope of the winter-mean kinetic energy spectrum computed from INALT60 for 350 km × 350 km regions every 100 km in both horizontal directions (Fig. 9f). For the 2012–17 period, the subgyre, as well as the AC, ARC, and the retroflection, are associated with

slopes steeper than $K^{-2.5}$, while the Agulhas ring path and the rest of the domain are associated with slopes shallower than K^{-2}. This and the former highlight further that the mixed layer instability is of key importance for the open-ocean submesoscale inverse cascade at the surface.

Besides the scale, where the cascade changes from forward to inverse, also the amplitude of the fluxes shows strong regional differences. The amplitude of the flux is largest in the region of the retroflection, strong in the subgyre and in the region of the ARC, weak in the Agulhas ring path, and very weak in the open ocean (Figs. 9a–c). An explanation for this spatial pattern might be that the fluxes are larger the stronger the submesoscale dynamics are and that the submesoscale dynamics are in turn stronger the stronger the mesoscale dynamics interact.

4. Conclusions and discussion

In this study, we show that mesoscale oceanic eddies are strengthened by the absorption of submesoscale vortices resulting from mixed layer baroclinic instability. As the absorption needs time to proceed, the strengthening occurs several months after the maximum of submesoscale kinetic energy in winter. The timing of the strengthening is coincident with the seasonal maximum

of mesoscale kinetic energy, indicating an importance of submesoscale flows for the mesoscale seasonal cycle. Surface downscale fluxes at the smallest resolved scales occur preferentially in frontogenetic regions.

We show this for the case of the Agulhas region by investigating the submesoscale kinetic energy cascade in two high-resolution ocean model simulations for the first time with a coarse-graining approach. In contrast to the classical spectral approach, the coarse-graining approach allows an easier mapping of the cascade and thus a better attribution of the cascade to processes. For the spatial-average of the ring path, we demonstrate that both approaches produce similar results, in particular for scales smaller than 40 km. At larger scales, the spectral approach is associated with weaker fluxes. We hypothesize that at these larger scales, the assumptions of homogeneous and isotropic turbulence, that need to be made for the spectral approach but are not made for the coarse-graining approach, are not valid and thus the coarse-graining results are likely to be more realistic. The coarse-graining approach comes in turn along with the limitations that it is costly in terms of computational power as well as data storage capacities. In this study, the scale flux is computed for scales of 300 km and smaller and only close to the surface. We assume that for these scales the effect of Earth's curvature on the flux computations can be neglected and thus that the chosen convolution kernel [Eq. (B1)] is a reasonable choice. Future research could compare the fluxes with those computed by a convolution on a sphere (Aluie 2019).

Submesoscale currents flux their kinetic energy to both larger (upscale) as well as to smaller horizontal scales (downscale). Strong upscale fluxes occur throughout the whole depth of the mixed layer in winter. We present several indications that these fluxes are partially attributable to the growth of mixed layer baroclinic instability driven features and their absorption by mesoscale eddies. First, the source of the upscale flux (the flux divergence with respect to the scale) is found to be largest in winter at scales around 15 km, where also the forward cascade changes to an inverse cascade in the ring path. These are typical scales of features that develop as a result of mixed layer baroclinic instability (Boccaletti et al. 2007; Fox-Kemper et al. 2008). This is consistent with Sasaki et al. (2014), who found at these scales a maximum of the spectrum of the vertical buoyancy flux which is, in the framework of the Lorenz energy cycle, a measure of the energy transfer from eddy potential to eddy kinetic energy and an indicator of baroclinic instability. Second, in a strongly eddying simulation that, however, does not resolve the mixed layer instability, these sources for the inverse cascade are almost absent and the mesoscale eddies are too weak. Third, a case study of mixed layer

instability driven features that are absorbed by an Agulhas ring shows an upscale flux of kinetic energy into the scale of the ring along its whole sidewall. Fourth, the maximum of scale kinetic energy flux shifts to larger scales after the submesoscale season accompanied by a coincident shift of the maximum in kinetic energy. This is consistent with the notion that the absorption of the smaller-scale features needs time to proceed. Further, this indicates that submesoscale flows affect the seasonal cycle of mesoscale eddy kinetic energy. Contradictory, Rieck et al. (2015) could reproduce the mesoscale seasonal cycle identified from AVISO with a non-submesoscale-resolving ocean simulation in large parts of the global ocean. However, in some regions, the month of the maximum of mesoscale eddy kinetic energy in their simulation differed from the one of the observations. The relevance of the submesoscales for the mesoscale seasonal cycle has to be investigated closer in the future. Fifth, the pattern of the wavelength of the most unstable mixed layer instability mode is similar to the one of the scale, where the inverse changes to a forward cascade, as well as the one of the slope of the kinetic energy spectrum. This indicates further the importance of the mixed layer instability for the submesoscale kinetic energy cascade.

Downscale fluxes at the smallest resolved scales (≈ 7 km) are found to be concentrated in frontogenetic regions in the upper 30 m of the ocean. In the Agulhas region, 61% of the surface downscale flux at a scale of 7 km occurs in regions with a frontogenetic tendency of more than 0.1 $[(\text{kg m}^{-3}) \text{ km}^{-1}]^2 \text{ day}^{-1}$. As far as we know, this is the first time that the collocation of frontal regions and downscale kinetic energy flux is explicitly shown in the literature. Our results are consistent with D'Asaro et al. (2011), who found enhanced kinetic energy dissipation in a front within the Kuroshio region. They attributed the dissipation to symmetric instability of the front. In our simulation, it is hard to attribute the downscale flux at 7 km to a specific process, as this scale marks the small-scale end of the resolved physics in the model and symmetric instability and other smaller-scale instabilities are only partially or not resolved in the simulation (e.g., Bachman and Taylor 2014). Further, the scale fluxes are computed based on the model solution that is affected by the (nonphysical) model dissipation at these and smaller scales. The impact of the model dissipation on the resulting scale kinetic energy flux might dominate the one of permitted frontal instabilities.

Our results are consistent with previous modeling studies for other regions. Capet et al. (2008) found for the California Current system an inverse cascade down to a wavelength (scale) of about 34 km (17 km) and supposed that the forward cascade occurs mainly at

fronts—which is shown here explicitly. Qiu et al. (2014) found for the North Pacific Subtropical Countercurrent a change from inverse to forward cascade in winter at wavelengths (scales) of 30 km (15 km). Moreover, they found a similar seasonal cycle of the inverse cascade with stronger upscale fluxes that extend to smaller scales in winter, and a transition of the scale of change to downscale fluxes to larger scales after the submesoscale season during the weakening of the frontal instabilities.

The computation of the scale kinetic energy flux is limited in that the fluxes are computed based on the model solutions and thus do not capture the effect of smaller scale flows. Although Capet et al. (2008) find no change in the scale where the inverse cascade changes to forward when they increased the horizontal resolution from 1.5 km to 750 m, they observe an increase of both upscale and downscale fluxes. We thus expect an increase in the amplitude of the fluxes when the model resolution is further increased.

Summarizing, our results show that the absorption of mixed layer eddies strengthen mesoscale eddies in the Agulhas region and that downscale kinetic energy fluxes occur preferentially in frontogenetic regions. A future study needs to investigate the relevance of the former for the mesoscale eddies. The large computational power and data storage capacities needed for the coarse-graining approach, when applied to such high-resolution model data, restricted the analysis here to mainly the surface ocean. This does not allow conclusions on the integral effect of the submesoscales on the mesoscales. As the involved mechanisms are generic, we expect that our findings, shown here for the ring path and the southwest Indian Ocean subgyre, hold for the global ocean. This needs to be checked. In particular in the ring path, besides the open-ocean submesoscale inverse cascade, the strength of the eddies is also impacted by the upstream dynamics in the retroflection and along the Agulhas bank. Although the comparison of INALT60 and INALT20r shows that, in the ring path, the mesoscale (>100 km) kinetic energy increases by 28%, if submesoscale flows are resolved, here we are not able to identify which part of this strengthening is attributable to the absorption of mixed layer eddies and which part to a better representation of the eddy formation at the Agulhas bank. If the upscale effect of eddies resulting from mixed layer instabilities is relevant for the mesoscales, this effect needs to be parameterized in coarse-resolution ocean models besides the restratifying effect of the mixed layer instability (e.g., Fox-Kemper et al. 2008). Further, it needs to be investigated which role the Charney type baroclinic instability (Capet et al. 2016) plays for the submesoscale kinetic energy cascade in the Agulhas region.

A further open question is, what effect the submesoscale dynamics have on Agulhas leakage and its impact on the Atlantic Ocean circulation? To address this question, longer integration periods and a larger submesoscale permitting domain are necessary. On the one-hand, the leakage might be increased due to important submesoscale contributions to the Agulhas cyclone formation. On the other hand, the submesoscale flows drive an exchange of Agulhas eddies with their surroundings (Sinha et al. 2019) that is of importance for the water masses that enter the Atlantic (Capuano et al. 2018).

APPENDIX A

The Computation of the Kinetic Energy Spectrum

Before the Fourier transformation of a horizontal field $F(x, y)$, where x and y are Cartesian coordinates in approximately zonal and meridional directions, the mean of F is subtracted and F is linearly detrended in both horizontal directions. Here, we investigate square-shaped domains with N data points within the side length. As the domain is not periodic, nor infinitely large, F is multiplied by a 2D Hanning window and the associated amplitude correction factor of 1.5. The Fourier transform of F is defined as

$$\hat{F}(k, l) = \frac{1}{(2\pi)^2} \int_{-\infty}^{\infty} \int_{-\infty}^{\infty} F(x, y) e^{-i(kx+ly)} \, dx \, dy,$$

where k and l are the zonal and meridional wavenumber components. The cumulative power spectral density of horizontal velocities is derived as

$$E(K) = \frac{1}{N^4} \int_0^K \frac{1}{2} (\hat{u}^*\hat{u} + \hat{v}^*\hat{v}) \, dK,$$

where $K = \sqrt{k^2 + l^2}$ is the isotropic wavenumber. The complex conjugate is denoted by * and u and v are the quasi-zonal and quasi-meridional velocity components. The Fourier transforms $\hat{u}$ and $\hat{v}$ are normalized by the area N^2 before the computation of the power spectral density. The velocity components are quasi-zonal and quasi-meridional, as the model output on a geographical grid needs to be interpolated onto a regular Cartesian grid to apply the Fourier analysis. The power spectral density of horizontal velocities, in the following referred to as the kinetic energy spectrum, is then given by $2\pi(dE/dK)$. For the time-mean kinetic energy spectrum, the spectrum is computed first for each model snapshot every fifth day and subsequently averaged over all spectra.

APPENDIX B

The Computation of the Scale Kinetic Energy Flux

The scale kinetic energy flux $\Pi(L)$ is the rate of transfer of kinetic energy from currents with scales smaller than a specific horizontal scale L to currents with scales larger than L. The flux divergence $T(L) = \partial\Pi/\partial L$ yields sources and sinks of $\Pi(L)$. While we use the term "flux divergence" throughout the paper, T is occasionally also referred to as the scale energy transfer as it is the source term in the budget of the power spectral kinetic energy density (e.g., Scott and Arbic 2007). Here, we use two methods for the computation of Π: a spectral and a coarse-graining approach.

a. Spectral approach

Energy is fluxed across scales by nonlinear interactions. The scale kinetic energy flux is usually derived using the integral of the Fourier transformed nonlinear advection term

$$\Pi_{\mathrm{sp}}(K) = -\rho_0 \int_K^\infty \hat{\mathbf{u}}_h^* \cdot (\widehat{\mathbf{u}_h \nabla_h \mathbf{u}_h})\, dK,$$

where $\mathbf{u}_h = (u, v)$ is the horizontal velocity vector. Negative values of Π_{sp} indicate an upscale flux of kinetic energy. The spectral approach is associated with several limitations. First, one has to assume that turbulence is isotropic and homogeneous. Second, a value for the flux at the small-scale end has to be assumed. Here, we use the common assumption of zero flux at the smallest investigated scales. Third, the region, for which the energy flux is computed, is not well defined due to the necessary windowing. Fourth, Π_{sp} is usually associated with noise leading to unreasonably high values of the flux divergence (e.g., Scott and Wang 2005).

b. Coarse-graining approach

In this study, we focus on an alternative approach for the scale kinetic energy flux computations based on coarse graining that is not associated with the above mentioned limitations of the spectral approach. The coarse-graining approach has been earlier applied to turbulence problems by Leonard (1975) and Germano (1992) and has been developed further by Eyink (2005). Aluie et al. (2018) applied the approach to a large-scale ocean general circulation model to investigate the scale energy flux between the oceanic mesoscale and large-scale circulation. Here, we study the energy cascade between the submesoscale and the mesoscale dynamics. In this section, we give a short overview of the derivation of scale energy flux based on Germano (1992) and Aluie et al. (2018) and describe how we apply it to our model outputs.

A horizontal field $F(x, y)$ is low-pass filtered by applying a convolution $\overline{F}(x, y) = C \times F(x, y)$ with a top-hat kernel

$$C(\mathbf{r}) = \begin{cases} 1/A, & \text{if } |\mathbf{r}| < L/2, \\ 0, & \text{otherwise}, \end{cases} \tag{B1}$$

where $A = \pi L^2/4$ is the circular normalization area of diameter L and $\mathbf{r}$ is the radial position vector. In other words, the low-pass-filtered field is the result of a circular two-dimensional running mean with diameter L that filters out all scales smaller than L from the original field $F(x, y)$. Applying the convolution to the rotating Boussinesq equations leads to the equations of motion for $\overline{\mathbf{u}}$, where $\mathbf{u} = (u, v, w)$ is the velocity vector with u, v, and the vertical component w. The form of the equations of motion does not change as the convolution is commutative with the spatial and temporal derivatives (Aluie et al. 2018). However, a new term arises from the nonlinear advection term:

$$\nabla \cdot \overline{\mathbf{u}\mathbf{u}} = \nabla \cdot \overline{\mathbf{u}}\,\overline{\mathbf{u}} + \nabla \cdot \overline{\tau}(\mathbf{u}, \mathbf{u}),$$

where $\overline{\tau}(\mathbf{u}, \mathbf{u}) = \overline{\mathbf{u}\mathbf{u}} - \overline{\mathbf{u}}\,\overline{\mathbf{u}}$ is the subfilter stress tensor. The term $\nabla \cdot \overline{\tau}(\mathbf{u}, \mathbf{u})$ is the force that the subfilter (small-scale) motions exert on the low-pass-filtered (large-scale) flow. To derive the large-scale kinetic energy budget, the scalar product of the momentum equations with $\rho_0\overline{\mathbf{u}}$ is computed. The respective contribution of the subfilter stress can be split into

$$\rho_0\overline{\mathbf{u}} \cdot [\nabla \cdot \overline{\tau}(\mathbf{u}, \mathbf{u})] = \nabla \cdot [\rho_0\overline{\mathbf{u}} \cdot \overline{\tau}(\mathbf{u}, \mathbf{u})] - \rho_0\overline{S} : \overline{\tau}(\mathbf{u}, \mathbf{u}),$$
$$\tag{B2}$$

where the colon is a tensor inner product. The first term on the right-hand side is the divergence of the transport

of large-scale kinetic energy by small-scale currents. This term does not contribute to a flux of kinetic energy across scales. The second term is the scale kinetic energy flux $\Pi_{cg} = -\rho_0 \overline{S} : \overline{\tau}(\mathbf{u}, \mathbf{u})$, where $\overline{S} = (\nabla \overline{\mathbf{u}} + \nabla \overline{\mathbf{u}}^T)/2$ is the large-scale strain tensor. The separation into both contributions is associated with a gauge freedom. Here we followed the separation suggested by Aluie et al. (2018) which has the advantage of a Galilean invariant definition for the scale kinetic energy flux. Negative values of Π_{cg} are again associated with upscale kinetic energy flux and positive with downscale. Neglecting the distribution of the vertical velocity component, the scale energy flux reduces to

$$\Pi_{cg}(\mathbf{x}) = -\rho_0[(\overline{u^2} - \overline{u}^2)\overline{u}_x + (\overline{uv} - \overline{u}\,\overline{v})(\overline{u}_y + \overline{v}_x) + (\overline{v^2} - \overline{v}^2)\overline{v}_y].$$

Note that the form of the horizontal Π_{cg} is similar to the one of the barotropic instability term that transfers energy between the Reynolds-average based mean and eddy kinetic energy reservoirs integrated over closed domains (e.g., Harrison and Robinson 1978).

The computation of Π_{cg} is much faster for regular grids and thus a constant convolution kernel C. The horizontal velocity components u and v are first interpolated onto the tracer grid points of the Arakawa C grid. The respective geographical coordinates are transformed into Cartesian coordinates using the European Petroleum Survey Group Geodesy numbers 4326 (World Geodetic System 1984) and 3395 (Cartesian). Subsequently, both u and v are linearly interpolated onto a regular grid with 1-km grid spacing before the horizontal convolution and the computations of Π_{cg} as well as Π_{sp} are performed. The computational cost of the convolution scales with L^2. Land cells are treated as cells with zero velocity, as suggested by Aluie et al. (2018). Π_{cg} is computed for the following length scales $L = 7, 10, 15, 20, 30, 45, 60, 100, 150, 200, 300$ km. We show that the results are useful for a computation of the flux divergence $T_{cg} = \partial \Pi_{cg}/\partial L$. Negative values of T_{cg} show a source for the upscale flux and positive a sink.

The length scale L used for the coarse-graining approach corresponds to half the wavelength λ used in the spectral approach. Elliptic features such as eddies imprint in the spectrum at a wavelength which is about twice their diameter. The good agreement of the scale kinetic energy flux at the smaller scales computed with the spectral and the coarse-graining approach (Fig. 3) confirms this relation.

REFERENCES

Aluie, H., 2019: Convolutions on the sphere: Commutation with differential operators. *Int. J. Geomath.*, **10**, 9, https://doi.org/10.1007/s13137-019-0123-9.

——, M. Hecht, and G. K. Vallis, 2018: Mapping the energy cascade in the north Atlantic Ocean: The coarse-graining approach. *J. Phys. Oceanogr.*, **48**, 225–244, https://doi.org/10.1175/JPO-D-17-0100.1.

Arakawa, A., and V. R. Lamb, 1977: Computational design of the basic dynamical processes of the UCLA general circulation model. *General Circulation Models of the Atmosphere*, J. Chang, Ed., Vol. 17, *Methods in Computational Physics: Advances in Research and Applications*, Academic Press, 173–265.

——, and Y.-J. G. Hsu, 1990: Energy conserving and potential-enstrophy dissipating schemes for the shallow water equations. *Mon. Wea. Rev.*, **118**, 1960–1969, https://doi.org/10.1175/1520-0493(1990)118<1960:ECAPED>2.0.CO;2.

Arbic, B. K., K. L. Polzin, R. B. Scott, J. G. Richman, and J. F. Shriver, 2013: On eddy viscosity, energy cascades, and the horizontal resolution of gridded satellite altimeter products. *J. Phys. Oceanogr.*, **43**, 283–300, https://doi.org/10.1175/JPO-D-11-0240.1.

Bachman, S. D., and J. R. Taylor, 2014: Modelling of partially-resolved oceanic symmetric instability. *Ocean Modell.*, **82**, 15–27, https://doi.org/10.1016/j.ocemod.2014.07.006.

Barkan, R., K. B. Winters, and S. G. Llewellyn Smith, 2015: Energy cascades and loss of balance in a reentrant channel forced by wind stress and buoyancy fluxes. *J. Phys. Oceanogr.*, **45**, 272–293, https://doi.org/10.1175/JPO-D-14-0068.1.

Beal, L. M., S. Elipot, A. Houk, and G. M. Leber, 2015: Capturing the transport variability of a western boundary jet: Results from the Agulhas Current Time-Series Experiment (ACT). *J. Phys. Oceanogr.*, **45**, 1302–1324, https://doi.org/10.1175/JPO-D-14-0119.1.

Bell, M. J., P. S. Peixoto, and J. Thuburn, 2017: Numerical instabilities of vector-invariant momentum equations on rectangular C-grids. *Quart. J. Roy. Meteor. Soc.*, **143**, 563–581, https://doi.org/10.1002/qj.2950.

Biastoch, A., C. W. Böning, and J. Lutjeharms, 2008: Agulhas leakage dynamics affects decadal variability in Atlantic overturning circulation. *Nature*, **456**, 489–492, https://doi.org/10.1038/nature07426.

——, J. V. Durgadoo, A. K. Morrison, E. Van Sebille, W. Weijer, and S. M. Griffies, 2015: Atlantic multi-decadal oscillation covaries with Agulhas leakage. *Nat. Commun.*, **6**, 10082, https://doi.org/10.1038/ncomms10082.

Blumen, W., 1978: Uniform potential vorticity flow: Part I. Theory of wave interactions and two-dimensional turbulence. *J. Atmos. Sci.*, **35**, 774–783, https://doi.org/10.1175/1520-0469(1978)035<0774:UPVFPI>2.0.CO;2.

Boccaletti, G., R. Ferrari, and B. Fox-Kemper, 2007: Mixed layer instabilities and restratification. *J. Phys. Oceanogr.*, **37**, 2228–2250, https://doi.org/10.1175/JPO3101.1.

Boebel, O., J. Lutjeharms, C. Schmid, W. Zenk, T. Rossby, and C. Barron, 2003: The cape cauldron: A regime of turbulent inter-ocean exchange. *Deep-Sea Res. II*, **50**, 57–86, https://doi.org/10.1016/S0967-0645(02)00379-X.

Boyd, J. P., 1992: The energy spectrum of fronts: Time evolution of shocks in Burger's equation. *J. Atmos. Sci.*, **49**, 128–139, https://doi.org/10.1175/1520-0469(1992)049<0128:TESOFT>2.0.CO;2.

Callies, J., and R. Ferrari, 2013: Interpreting energy and tracer spectra of upper-ocean turbulence in the submesoscale range (1–200 km). *J. Phys. Oceanogr.*, **43**, 2456–2474, https://doi.org/10.1175/JPO-D-13-063.1.

Capet, X., J. C. McWilliams, M. J. Molemaker, and A. Shchepetkin, 2008: Mesoscale to submesoscale transition in the California Current System. Part III: Energy balance and flux. *J. Phys. Oceanogr.*, **38**, 2256–2269, https://doi.org/10.1175/2008JPO3810.1.

——, G. Roullet, P. Klein, and G. Maze, 2016: Intensification of upper-ocean submesoscale turbulence through Charney baroclinic instability. *J. Phys. Oceanogr.*, **46**, 3365–3384, https://doi.org/10.1175/JPO-D-16-0050.1.

Capuano, T. A., S. Speich, X. Carton, and B. Blanke, 2018: Mesoscale and submesoscale processes in the Southeast Atlantic and their impact on the regional thermohaline structure. *J. Geophys. Res. Oceans*, **123**, 1937–1961, https://doi.org/10.1002/2017JC013396.

Charney, J. G., 1971: Geostrophic turbulence. *J. Atmos. Sci.*, **28**, 1087–1095, https://doi.org/10.1175/1520-0469(1971)028<1087:GT>2.0.CO;2.

Chelton, D. B., R. A. Deszoeke, M. G. Schlax, K. El Naggar, and N. Siwertz, 1998: Geographical variability of the first baroclinic Rossby radius of deformation. *J. Phys. Oceanogr.*, **28**, 433–460, https://doi.org/10.1175/1520-0485(1998)028<0433:GVOTFB>2.0.CO;2.

Cronin, M., 1996: Eddy-mean flow interaction in the Gulf Stream at 68°W. Part II: Eddy forcing on the time-mean flow. *J. Phys. Oceanogr.*, **26**, 2132–2151, https://doi.org/10.1175/1520-0485(1996)026<2132:EMFIIT>2.0.CO;2.

D'Asaro, E., C. Lee, L. Rainville, R. Harcourt, and L. Thomas, 2011: Enhanced turbulence and energy dissipation at ocean fronts. *Science*, **332**, 318–322, https://doi.org/10.1126/science.1201515.

Debreu, L., C. Vouland, and E. Blayo, 2008: AGRIF: Adaptive grid refinement in Fortran. *Comput. Geosci.*, **34**, 8–13, https://doi.org/10.1016/j.cageo.2007.01.009.

de Ruijter, W., A. Biastoch, S. Drijfhout, J. Lutjeharms, R. Matano, T. Pichevin, P. Van Leeuwen, and W. Weijer, 1999: Indian-Atlantic interocean exchange: Dynamics, estimation and impact. *J. Geophys. Res. Oceans*, **104**, 20 885–20 910, https://doi.org/10.1029/1998JC900099.

Ducousso, N., J. Le Sommer, J.-M. Molines, and M. Bell, 2017: Impact of the "symmetric instability of the computational kind" at mesoscale-and submesoscale-permitting resolutions. *Ocean Modell.*, **120**, 18–26, https://doi.org/10.1016/j.ocemod.2017.10.006.

Eady, E. T., 1949: Long waves and cyclone waves. *Tellus*, **1**, 33–52, https://doi.org/10.3402/tellusa.v1i3.8507.

Eyink, G. L., 2005: Locality of turbulent cascades. *Physica D*, **207**, 91–116, https://doi.org/10.1016/j.physd.2005.05.018.

Farrow, D. E., and D. P. Stevens, 1995: A new tracer advection scheme for Bryan and Cox type ocean general circulation models. *J. Phys. Oceanogr.*, **25**, 1731–1741, https://doi.org/10.1175/1520-0485(1995)025<1731:ANTASF>2.0.CO;2.

Ferrari, R., and C. Wunsch, 2009: Ocean circulation kinetic energy: Reservoirs, sources, and sinks. *Annu. Rev. Fluid Mech.*, **41**, 253–282, https://doi.org/10.1146/annurev.fluid.40.111406.102139.

Fox-Kemper, B., R. Ferrari, and R. Hallberg, 2008: Parameterization of mixed layer eddies. Part I: Theory and diagnosis. *J. Phys. Oceanogr.*, **38**, 1145–1165, https://doi.org/10.1175/2007JPO3792.1.

Germano, M., 1992: Turbulence: The filtering approach. *J. Fluid Mech.*, **238**, 325–336, https://doi.org/10.1017/S0022112092001733.

Griffies, S. M., and Coauthors, 2009: Coordinated Ocean-Ice Reference Experiments (COREs). *Ocean Modell.*, **26**, 1–46, https://doi.org/10.1016/j.ocemod.2008.08.007.

Harrison, D., and A. Robinson, 1978: Energy analysis of open regions of turbulent flows—Mean eddy energetics of a numerical ocean circulation experiment. *Dyn. Atmos. Oceans*, **2**, 185–211, https://doi.org/10.1016/0377-0265(78)90009-X.

Held, I. M., R. T. Pierrehumbert, S. T. Garner, and K. L. Swanson, 1995: Surface quasi-geostrophic dynamics. *J. Fluid Mech.*, **282**, 1–20, https://doi.org/10.1017/S0022112095000012.

Hollingsworth, A., P. Kållberg, V. Renner, and D. Burridge, 1983: An internal symmetric computational instability. *Quart. J. Roy. Meteor. Soc.*, **109**, 417–428, https://doi.org/10.1002/qj.49710946012.

Hoskins, B. J., 1982: The mathematical theory of frontogenesis. *Annu. Rev. Fluid Mech.*, **14**, 131–151, https://doi.org/10.1146/annurev.fl.14.010182.001023.

Kjellsson, J., and L. Zanna, 2017: The impact of horizontal resolution on energy transfers in global ocean models. *Fluids*, **2**, 45, https://doi.org/10.3390/fluids2030045.

Klein, P., B. L. Hua, G. Lapeyre, X. Capet, S. Le Gentil, and H. Sasaki, 2008: Upper ocean turbulence from high-resolution 3D simulations. *J. Phys. Oceanogr.*, **38**, 1748–1763, https://doi.org/10.1175/2007JPO3773.1.

——, and Coauthors, 2019: Ocean-scale interactions from space. *Earth Space Sci.*, **6**, 795–817, https://doi.org/10.1029/2018ea000492.

Kraichnan, R. H., 1967: Inertial ranges in two-dimensional turbulence. *Phys. Fluids*, **10**, 1417–1423, https://doi.org/10.1063/1.1762301.

Lapeyre, G., 2017: Surface quasi-geostrophy. *Fluids*, **2**, 7, https://doi.org/10.3390/fluids2010007.

——, and P. Klein, 2006: Dynamics of the upper oceanic layers in terms of surface quasigeostrophy theory. *J. Phys. Oceanogr.*, **36**, 165–176, https://doi.org/10.1175/JPO2840.1.

Large, W. G., and S. Yeager, 2009: The global climatology of an interannually varying air–sea flux data set. *Climate Dyn.*, **33**, 341–364, https://doi.org/10.1007/s00382-008-0441-3.

Leonard, A., 1975: Energy cascade in large-eddy simulations of turbulent fluid flows. *Advances in Geophysics*, Vol. 18, Academic Press, 237–248, https://doi.org/10.1016/S0065-2687(08)60464-1.

Lübbecke, J. F., J. V. Durgadoo, and A. Biastoch, 2015: Contribution of increased Agulhas leakage to tropical Atlantic warming. *J. Climate*, **28**, 9697–9706, https://doi.org/10.1175/JCLI-D-15-0258.1.

Lutjeharms, J., 2007: Three decades of research on the greater Agulhas Current. *Ocean Sci.*, **3**, 129–147, https://doi.org/10.5194/os-3-129-2007.

——, and I. Ansorge, 2001: The Agulhas return current. *J. Mar. Syst.*, **30**, 115–138, https://doi.org/10.1016/S0924-7963(01)00041-0.

——, O. Boebel, and H. Rossby, 2003: Agulhas cyclones. *Deep-Sea Res. II*, **50**, 13–34, https://doi.org/10.1016/S0967-0645(02)00378-8.

Ma, X., and Coauthors, 2016: Western boundary currents regulated by interaction between ocean eddies and the atmosphere. *Nature*, **535**, 533–537, https://doi.org/10.1038/nature18640.

Madec, G., and NEMO Team, 2016: NEMO ocean engine. Note du Pôle de modélisation de l'Institut Pierre-Simon Laplace 27, 386 pp., https://www.nemo-ocean.eu/wp-content/uploads/NEMO_book.pdf.

Molemaker, M. J., and J. C. McWilliams, 2010: Local balance and cross-scale flux of available potential energy. *J. Fluid Mech.*, **645**, 295–314, https://doi.org/10.1017/S0022112009992643.

Qiu, B., S. Chen, P. Klein, H. Sasaki, and Y. Sasai, 2014: Seasonal mesoscale and submesoscale eddy variability along the north Pacific subtropical countercurrent. *J. Phys. Oceanogr.*, **44**, 3079–3098, https://doi.org/10.1175/JPO-D-14-0071.1.

Renault, L., M. J. Molemaker, J. C. McWilliams, A. F. Shchepetkin, F. Lemarié, D. Chelton, S. Illig, and A. Hall, 2016: Modulation of wind work by oceanic current interaction with the atmosphere. *J. Phys. Oceanogr.*, **46**, 1685–1704, https://doi.org/10.1175/JPO-D-15-0232.1.

Rhines, P. B., 1975: Waves and turbulence on a beta-plane. *J. Fluid Mech.*, **69**, 417–443, https://doi.org/10.1017/S0022112075001504.

Rieck, J. K., C. W. Böning, R. J. Greatbatch, and M. Scheinert, 2015: Seasonal variability of eddy kinetic energy in a global high-resolution ocean model. *Geophys. Res. Lett.*, **42**, 9379–9386, https://doi.org/10.1002/2015GL066152.

Rubio, A., B. Blanke, S. Speich, N. Grima, and C. Roy, 2009: Mesoscale eddy activity in the southern Benguela upwelling system from satellite altimetry and model data. *Prog. Oceanogr.*, **83**, 288–295, https://doi.org/10.1016/j.pocean.2009.07.029.

Sasaki, H., P. Klein, B. Qiu, and Y. Sasai, 2014: Impact of oceanic-scale interactions on the seasonal modulation of ocean dynamics by the atmosphere. *Nat. Commun.*, **5**, 5636, https://doi.org/10.1038/ncomms6636.

Schubert, R., A. Biastoch, M. F. Cronin, and R. J. Greatbatch, 2018: Instability-driven benthic storms below the separated Gulf Stream and the North Atlantic Current in a high-resolution ocean model. *J. Phys. Oceanogr.*, **48**, 2283–2303, https://doi.org/10.1175/JPO-D-17-0261.1.

——, F. U. Schwarzkopf, B. Baschek, and A. Biastoch, 2019: Submesoscale impacts on mesoscale Agulhas dynamics. *J. Adv. Model. Earth Syst.*, **11**, 2745–2767, https://doi.org/10.1029/2019MS001724.

Schwarzkopf, F. U., and Coauthors, 2019: The INALT family–A set of high-resolution nests for the Agulhas Current system within global NEMO ocean/sea-ice configurations. *Geosci. Model Dev.*, **12**, 3329–3355, https://doi.org/10.5194/gmd-12-3329-2019.

Scott, R. B., and F. Wang, 2005: Direct evidence of an oceanic inverse kinetic energy cascade from satellite altimetry. *J. Phys. Oceanogr.*, **35**, 1650–1666, https://doi.org/10.1175/JPO2771.1.

——, and B. K. Arbic, 2007: Spectral energy fluxes in geostrophic turbulence: Implications for ocean energetics. *J. Phys. Oceanogr.*, **37**, 673–688, https://doi.org/10.1175/JPO3027.1.

Sinha, A., D. Balwada, N. Tarshish, and R. Abernathey, 2019: Modulation of lateral transport by submesoscale flows and inertia gravity waves. *J. Adv. Model. Earth Syst.*, **11**, 1039–1065, https://doi.org/10.1029/2018MS001508.

Soufflet, Y., P. Marchesiello, F. Lemarié, J. Jouanno, X. Capet, L. Debreu, and R. Benshila, 2016: On effective resolution in ocean models. *Ocean Modell.*, **98**, 36–50, https://doi.org/10.1016/j.ocemod.2015.12.004.

Stöckli, R., E. Vermote, N. Saleous, R. Simmon, and D. Herring, 2005: The Blue Marble: Next Generation—A true color earth dataset including seasonal dynamics from MODIS. NASA Earth Observatory, https://earthobservatory.nasa.gov/features/BlueMarble.

Stone, P. H., 1970: On non-geostrophic baroclinic stability: Part II. *J. Atmos. Sci.*, **27**, 721–726, https://doi.org/10.1175/1520-0469(1970)027<0721:ONGBSP>2.0.CO;2.

Storch, J.-S., C. Eden, I. Fast, H. Haak, D. Hernández-Deckers, E. Maier-Reimer, J. Marotzke, and D. Stammer, 2012: An estimate of the Lorenz energy cycle for the world ocean based on the 1/10° STORM/NCEP simulation. *J. Phys. Oceanogr.*, **42**, 2185–2205, https://doi.org/10.1175/JPO-D-12-079.1.

Tsujino, H., and Coauthors, 2018: JRA-55 based surface dataset for driving ocean–sea-ice models (JRA55-do). *Ocean Modell.*, **130**, 79–139, https://doi.org/10.1016/j.ocemod.2018.07.002.

Tulloch, R., J. Marshall, C. Hill, and K. S. Smith, 2011: Scales, growth rates, and spectral fluxes of baroclinic instability in the ocean. *J. Phys. Oceanogr.*, **41**, 1057–1076, https://doi.org/10.1175/2011JPO4404.1.

Webb, D. J., B. A. De Cuevas, and C. S. Richmond, 1998: Improved advection schemes for ocean models. *J. Atmos. Oceanic Technol.*, **15**, 1171–1187, https://doi.org/10.1175/1520-0426(1998)015<1171:IASFOM>2.0.CO;2.

Weijer, W., W. P. De Ruijter, A. Sterl, and S. S. Drijfhout, 2002: Response of the Atlantic overturning circulation to South Atlantic sources of buoyancy. *Global Planet. Change*, **34**, 293–311, https://doi.org/10.1016/S0921-8181(02)00121-2.

Zalesak, S. T., 1979: Fully multidimensional flux-corrected transport algorithms for fluids. *J. Comput. Phys.*, **31**, 335–362, https://doi.org/10.1016/0021-9991(79)90051-2.